Retrieving Leaf Area Index With a Neural Network Method: Simulation and Validation

Hongliang Fang and Shunlin Liang, *Senior Member, IEEE*

Abstract—Leaf area index (LAI) is a crucial biophysical parameter that is indispensable for many biophysical and climatic models. A neural network algorithm in conjunction with extensive canopy and atmospheric radiative transfer simulations is presented in this paper to estimate LAI from Landsat-7 Enhanced Thematic Mapper Plus data. Two schemes were explored; the first was based on surface reflectance, and the second on top-of-atmosphere (TOA) radiance. The implication of the second scheme is that atmospheric corrections are not needed for estimating the surface LAI. A soil reflectance index (SRI) was proposed to account for variable soil background reflectances. Ground-measured LAI data acquired at Beltsville, MD were used to validate both schemes. The results indicate that both methods can be used to estimate LAI accurately. The experiments also showed that the use of SRI is very critical.

Index Terms—Enhanced Thematic Mapper Plus (ETM+), leaf area index (LAI), neural networks (NNs), radiative transfer, soil reflectance index (SRI).

I. INTRODUCTION

LAND SURFACE properties and processes play an important role in the modeling of global climate change over time. Land surface properties are characterized by several essential parameters such as the type of cover, leaf area index (LAI), roughness length, and albedo. They are fundamental in determining water and energy exchanges between the land surface and the atmosphere in order to predict precipitation and surface radiation. Important processes such as canopy interception, evapotranspiration, and net photosynthesis are directly proportional to LAI [1]. LAI also is an important input parameter to many climate and ecological models to quantify these processes. For example, the Global Climate Observation System (GCOS) and the Global Terrestrial Observation System (GTOS) requires a LAI accuracy of ±0.2 to 1.0 for terrestrial climate modeling [2].[1]

Satellite remote sensing provides a unique way to obtain LAI over large areas [3]. For example, the Moderate Resolution Imaging Spectroradiometer (MODIS) LAI is a 1-km global data product updated once each eight-day period throughout the year. The Multi-angle Imaging Spectroradiometer (MISR) LAI has a spatial resolution of 1.1 km and also is updated every eight days. Current methods for estimating LAI from optical remotely sensed data are classified into several categories

[4]: 1) using the empirical relationship of LAI and vegetation indices (VI); 2) through the inversion of a radiative transfer (RT) model; 3) lookup table (LUT) method; and 4) neural network (NN) algorithms. Although the VI approach is simple, it is usually sensitive to soil and atmospheric conditions as well as measurement geometries and spatial resolutions and thus no unique relationship between LAI and VI is universally applicable [5]. The RT model inversion method, though more complex, describes the physical process of radiance transfer in the soil–vegetation system and is thus more general in application. The MODIS LAI product is being derived mainly with the LUT method and, for extreme conditions, the backup VI method [6]–[8]. A similar strategy is applied by MISR to derive LAI [9]. The POLarization and Directionality of the Earth's Reflectances (POLDER) data have been used to estimate LAI by inverting a simple soil–vegetation reflectance model over limited regions [10], [11]. Unfortunately, the conventional RT model inversion with an iterative process is both time consuming and difficult to use on regional and global scales [12]. Both the LUT and NN methods can speed up the inversion process significantly although they are still dependent upon the accuracy of biophysically based RT models. They are easy to use, since most of the complications lie in generating the database [13] and the algorithms could be run separately.

The general process of an NN inversion may be outlined as follows: 1) given a set of empirical environmental, leaf, canopy, and soil parameters, determine the set of canopy reflectances with a forward RT model; 2) initiate the NN training (or learning) process with part of the lookup table obtained in the first step, and establish the relationship between the input data and the output reflectances; 3) check the NN training with the other part of the LUT data or ground measurements; and 4) apply the trained and checked NN model to a new scenario to predict output parameters. The LUT must be general enough to include all the possible variations.

In this study, we examined two LAI retrieval schemes with an NN method and apply it to retrieve LAI from Landsat Enhanced Thematic Mapper Plus (ETM+) imagery. The first scheme retrieved LAI from atmospherically corrected surface reflectances; the second one from top-of-atmosphere (TOA) raw radiances detected by the ETM+ sensor. The second approach was suggested by the previous study [14], which used the TOA reflectance to estimate LAI with a neural network method. No atmospheric correction was applied, instead, the effective green-band reflectance at the TOA was used directly in [14] to estimate LAI. Turner *et al.* [15] have also tested the applicability of using raw radiance values when they assessed LAI–VI relationships across vegetation types. In their study

[1]Site visited in December 2001.

[15], the VIs were derived from raw digital numbers (DNs), radiances, TOA reflectances, and atmospherically corrected reflectances. It is meaningful, therefore, to test the relationship between TOA radiance and surface LAI with the neural network method. The similar idea has been proposed [16] to estimate land surface broadband albedo directly from MODIS imagery.

For each scheme, a database was created through RT model simulation. The structures of these two databases are identical except for the fact that the second database has incorporated atmospheric effects. Previous researchers as well as our tests have identified soil background reflectance as one of the most sensitive parameters affecting LAI inversion. In most of the current NN training experiments, randomly selected soil reflectance was used to construct the LUT. It is believed that the use of more realistic soil reflectance data would greatly improve LAI estimates. This paper makes use of the soil reflectance derived from the satellite data in order to drive the RT model, construct the databases and train the neural network. For comparison with other soil reflectance options, three additional soil reflectance scenarios were tested.

The following section introduces the RT model and the principles of the neural network method. The concept of the soil reflectance index (SRI), database construction and the neural network training procedure are then discussed in the methodology. The predicted LAI with both reflectance and radiance derived from ETM+ data will be described and validated with field measurements in the results and analysis section.

II. BACKGROUND

We intend to estimate LAI through the inversion of an RT model and apply this method to invert LAI from Landsat ETM+ reflectance and radiance data. In this section, we introduce the RT model, the data, and the NN method that were used.

A. Creating the LUT With an RT Model

Creating an appropriate LUT is the first step in the use of the NN algorithm to retrieve surface biophysical parameters. RT models relate the fundamental surface parameters (e.g., LAI and leaf optical properties) to scene reflectance for a given sun-surface-sensor geometry. As mentioned before, the main deficiency of the radiative transfer equation is the complexity inherent in its parameter inversion, which becomes a major barrier when large amounts of satellite data are used. This is one reason why simple radiative transfer models are often used [17], [18]. It is not our intention to review and compare all of these models. Instead, we focus on a common turbid medium model—the Markov chain reflectance model (MCRM) developed by Kuusk [19]. The MCRM calculates the angular distribution of canopy reflectance for different nadir angles for a given azimuth and wavelength [19]. This model incorporates the Markov properties of stand geometry into an analytical multispectral canopy reflectance model [20].

The canopy structure parameters include the green leaf area index, the ratio of leaf linear dimension to canopy height (S_L), the Markov parameter describing clumping (λ_z), and two parameters describing the leaf orientation distribution: the eccentricity of the leaf angle distribution (e) and the mean leaf angle

TABLE I
PARAMETER VALUES USED TO ESTABLISH THE CANOPY
REFLECTANCE DATABASE

PARAMETERS	VALUES	SOURCES
Solar zenith angle	10°, 20°, 30°, 40°, 50°, 60°, and 70°	
Angstrom turbidity factor	0.1	[22]
Leaf area index	0 ~ 10.0 by 0.1	
Leaf linear dimension/canopy height ratio	0.15	[22]
Markov parameter describing clumping	0.8	[23]
Eccentricity of the leaf angle distribution	0.0	[22]
Mean leaf angle of the elliptical LAD	0.0	[22]
Chlorophyll AB concentration	46.9	[23]
Leaf equivalent water thickness	0.01	[45]
Leaf protein content	0.001	[45]
Leaf cellulose and lignin content	0.002	[45]
Leaf structure parameter	1.88	[22]
Weight of the 1st Price function	0.01, 0.05, 0.1, 0.15, 0.2, 0.25, 0.3, 0.4, 0.5, 0.6, 0.8, 1	
Weight of the 2nd Price function	0.02	[10]
Weight of the 3rd, and 4th Price function	0.0	[10]

of the elliptical leaf angle distribution (θ_m). The leaf biochemical parameters include the leaf chlorophyll $a + b$ concentration (C_{ab}), protein content (C_p), cellulose + lignin content (C_c), structure parameter (N), the ratio of refractive indices of the leaf surface wax and internal materials (C_n), and the equivalent water thickness (C_w). Soil spectral and directional properties are described by a spectral model [21] in which four parameters give the proportion of each of the four spectral terms, r_{s1}, r_{s2}, r_{s3}, and r_{s4}. In this study, a nadir viewing angle represents the view of Landsat ETM+. There are two extra parameters: the first one is the solar zenith angle (θ_1) that is acquired from the Landsat ETM+ header file on each date; the second is the Angstrom turbidity factor, which accounts for the atmospheric turbidity and is set to 0.1 throughout this paper [22]. All of the input parameters are listed in Table I.

Soil reflectance, especially for small LAI values, is one of the most sensitive parameters in canopy reflectance models [23]. However, when LAI increases (>3), the importance of the soil background decreases [10]. Different researchers have used various ways to deal with the soil reflectance in RT model simulation. These methods can be grouped into four categories. The first group uses the field measured soil reflectance data. For example, the soil reflectance in one of the studies [14] was obtained from field measurements corresponding to medium-dark and medium-bright soils. When Abuelgasim et al. [24] inverted the geometric optical model of Li and Strahler [25], sunlit background reflectance in the red band was chosen to represent the typical reflectance observed in this region (about 0.24 to 0.31). Qi et al. [26] also used measured soil optical properties to invert the SAIL model. The second approach uses the soil reflectances from a soil spectral library. For example, Broge and Leblanc [27] used minimum and maximum soil reflectances from some representative soils to create the LUT. The third approach uses randomly generated soil reflectances. For example, Kimes et al. [13] defined a soil parameter (S), and soil reflectances in green,

red, and near-infrared (NIR) bands were calculated as $S * 0.2$, $S * 0.25$, and $S * 0.3$, respectively. The final group uses reflectances derived from the soil line. For example, the soil reflectance in the red band is randomly generated (between 0.02 and 0.40) [28] where the soil reflectance for the NIR was deduced using the soil line ($\rho_{\mathrm{NIR}} = 1.253\rho_R + 0.030$). It should be noted that the soil line be obtained *a priori* [28].

Generally, using field-measured soil reflectance is the most accurate approach if the data are available. Reflectances from a soil spectral library may not represent real conditions in the field. Randomly generated or soil line reflectances are appropriate when they are applied to particular soil background properties, since they are derived from empirical observations. The SRI that will be introduced and used in this paper is determined from the soil line derived directly from satellite imagery.

B. NN Method

Neural networks provide a very efficient tool to establish the relationship between a simulated reflectance field and the corresponding biophysical variables of interest as demonstrated before [14], [28]–[30]. Smith [11] inverted a simple multiple scattering model to estimate LAI from reflectances at three wavelengths that were subsequently used to train an NN that was applied to satellite observations. Gong *et al.* [31] employed an error back-propagation feed-forward neural network program to invert LAI and leaf area density from a canopy reflectance model [32]. The test results showed that a relative error between 1% and 5% or better was achievable for retrieving one parameter at a time or two parameters simultaneously [31]. Most of the previous work [14], [26], [31] made use of the simulated database from an RT model for both the training and checking purposes, i.e., part of the simulated data were used for training and the other part for testing. A significant disadvantage of checking with simulated data is that the simulated data may not be representative of the real environmental conditions. It is more desirable to apply the training results to reflectance data derived from satellite observations, and calibrate the results with the field-measured data.

The training process is usually computationally intensive. Since some of the satellite bands are closely related, only those bands that have the largest information content are applied in the training iteration. The commonly used bands are green, red, and NIR. The normalized difference vegetation index (NDVI) has also been used in many studies. NDVI is calculated as

$$\mathrm{NDVI} = (\rho_{\mathrm{NIR}} - \rho_R)/(\rho_{\mathrm{NIR}} + \rho_R) \qquad (1)$$

where ρ_R and ρ_{NIR} are the reflectances of the red and the NIR bands (bands 3 and 4 for Landsat ETM+), respectively. The benefit of using NDVI is that it amplifies the inherent information in both red and NIR bands through the division operation. Since NDVI integrates the information content of both red and NIR, Smith [14] only used green band (0.55 μm) reflectances and NDVI in the input training process. Simulations were made using three POLDER spectral bands (green, red, and NIR) with the central wavelengths at 443, 670, and 865 nm, respectively [13]. Some researchers used both red and NIR wavelengths in the training process [28], while others used red, NIR, and NDVI [26]. The effect of different band combinations—NDVI as a separate band—will be discussed later.

III. METHODOLOGY

Our data were acquired at an experimental site at the U.S. Department of Agriculture, Beltsville Agricultural Research Center (BARC) located in Beltsville, MD (a detailed description of this site can be found in [23]). Four clear Landsat ETM+ images (May 11, 2000, October 2, 2000, April 28, 2001 and August 2, 2001) have been obtained. The ground resolution of the ETM+ data is 30 m. During the four Landsat-7 overpasses, it was clear and cloudless, and field campaigns were carried out. Surface reflectance was measured with a FieldSpec Pro device and processed with the ViewSpec Pro software from Analytical Spectral Devices (ASD) [33]. LAI was measured with the LAI-2000 [34] in twilights or one to three days apart when it was cloudy. Field measurements were conducted over typical land cover types such as alfalfa, wheat, corn, grass, soybean, and forest. To obtain green LAI for forests, the full canopy LAI was subtracted by the leafless LAI measured on March 20, 2001.

The ETM+ DNs were converted to radiances by [35]

$$L_s = (\mathrm{DN\text{-}Offset})/\mathrm{Gain} \qquad (2)$$

where L_s is the at-satellite spectral radiance for a given spectral band (Wm^{-2} sr^1μm^{-1}). The offsets and gains were available from the sensor metadata. The ETM+ data were atmospherically corrected using a radiative transfer package—MODTRAN 4.0—to obtain ground reflectance [36]. The MODTRAN input parameters, mainly water vapor content and aerosol optical thickness, were acquired from sunphotometers [37]. The ground surface was assumed to be Lambertian. Heterogeneous haze and aerosols were processed with the cluster match method introduced in [38]. Our validation work with the field data has proved the ETM+ reflectances were very accurate [39]. Fifty-one LAI field measurements were obtained for different large homogeneous sites. For each LAI point, surface reflectances were derived from the atmospherically corrected Landsat ETM+ data. Because the traditional empirical vegetation index approach, such as using NDVI, was not appropriate for this study area [23], the neural network approach to retrieve LAI was investigated.

A. SRI

The concept of soil reflectance index is evolved from the soil line. The linear relationship between red and NIR bare soil reflectances describes the soil line, which is widely used for the interpretation of remotely sensed data [40]. Some authors assume that all soil types might be represented by a unique "global" soil line, while Huete [41] points out that specific soil lines better describe the optical properties of individual soil types. The formula for a soil line follows

$$\rho_{\mathrm{NIR}} = \alpha\rho_R + \beta \qquad (3)$$

where ρ_R and ρ_{NIR} are the reflectances in the red and near-infrared bands, respectively, and α and β are the slope and intercept, respectively, of the soil line. The soil line slope and intercept vary from one time to another. In this work, the soil line parameters for each date were determined from the red–NIR spectral space. Table II shows the soil line parameters for various dates. The intercept (β) is not a single point, instead, a buffer

TABLE II
SOIL LINE PARAMETERS EXTRACTED FROM VARIOUS DATES. L_1 AND L_2 ARE THE LOWER AND UPPER PERCENTILE OF THE REFLECTANCE OF PIXELS IN BAND 3 TO CALCULATE THE MINIMUM AND MAXIMUM SOIL REFLECTANCE WHICH IS USED FOR SRI

DATES	SLOPE (α)	INTERCEPT (β)	L_1	L_2
May 11, 2000	1.0	0.02~0.08	0.01	0.02
Oct 2, 2000	1.03	0.008~0.08	0.02	0.02
Apr 28, 2001	1.1	0.008~0.08	0.01	0.02
Aug 2, 2001	1.05	0.008~0.08	0.01	0.02

range is given. (A more descriptive name might be soil pixel "strip.") All pixels located in this buffer zone are treated as soil pixels. Fig. 1 is an example of the soil pixel strip obtained from the imagery of May 11, 2000.

To calculate the SRI, minimum and maximum reflectances of the soil line must be calculated first, which are derived from the mean values of the lower and upper cluster of soil pixels using

$$\rho_1 = \text{Mean}(S_1) \quad \rho_2 = \text{Mean}(S_2) \tag{4}$$

and

$$S_1 = \forall \ (\rho - \rho_{G\min})/(\rho_{G\max} - \rho_{G\min}) < L_1$$
$$S_2 = \forall \ (\rho_{G\max} - \rho)/(\rho_{G\max} - \rho_{G\min}) < L_2 \tag{5}$$

where ρ_1 and ρ_2 are the minimum and maximum reflectances derived from the soil line. $\{S_1\}$ and $\{S_2\}$ are the lower and upper clusters of soil pixels used to calculate ρ_1 and ρ_2. $\rho_{G\min}$, $\rho_{G\max}$ are the global minimum and maximum reflectances from the soil line. L_1, L_2 are two boundary percentiles. The lower and upper percentiles for calculating the minimum and maximum reflectances are listed in Table II. For this analysis, both S_1 and S_2 were identified manually in the R-NIR space (Fig. 1), but they are not too difficult to be determined automatically. For simplification, S_1 and S_2 were decided based on the red band reflectance with (5).

Having determined the soil line from the R-NIR space, the SRI is defined as

$$\text{SRI} = \frac{\rho_s - \rho_1}{(\rho_2 - \rho_1)} \tag{6}$$

where ρ_1 and ρ_2 are the minimum and maximum red reflectances, respectively, on the soil line determined in (4), and ρ_s is the red band soil reflectance. Consequently, the soil background reflectance for each pixel can be calculated by

$$\rho_{is} = \rho_{i1} + (\rho_{i2} - \rho_{i1}) * \text{SRI} \tag{7}$$

where ρ_{i1} and ρ_{i2} are the minimum and maximum soil reflectances, respectively, at band i.

The soil reflectance index is a new concept introduced in this study. Our objective is to represent soil reflectance in a simple way by using the SRI. In so doing, the MCRM model only needs minor modifications and its computations will be simplified.

B. Companion Methods to Calculate Soil Reflectance

In addition to the SRI method introduced above, other methods can be used to calculate the soil reflectance depending
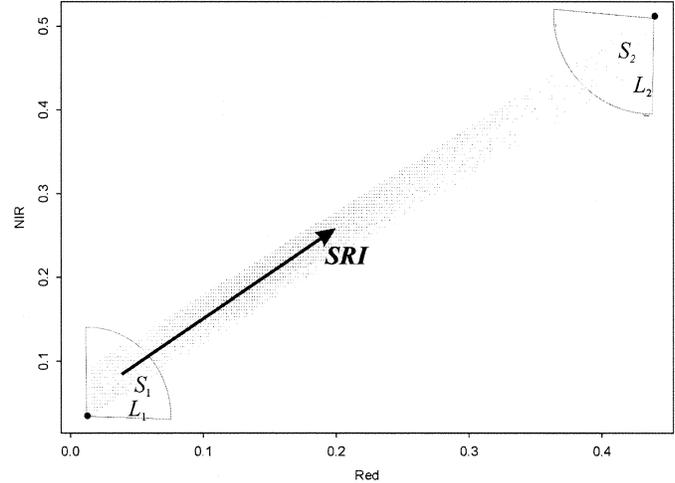

Fig. 1. Reflectance of soil pixels in red and NIR bands. S_1 (or S_2) are bounded by the contour representing an area within L_1 (or L_2) from the global minimum $\rho_{G\min}$ (or maximum $\rho_{G\max}$) reflectance.

on various application scenarios. In the following part, some of them will be elaborated on.

1) Scenario 1 (SN1): MCRM has two spectral soil parameters (r_{s1} and r_{s2}) and two directional soil parameters (r_{s3} and r_{s4}). The soil reflectance reads

$$\rho_s(\lambda, \theta_1, \theta_2, \phi) = (r_{s1}\varphi_1(\lambda) + r_{s1}\varphi_1(\lambda))$$
$$\cdot (1 + r_{s3}\theta_1\theta_2\cos\phi + r_{s4}\theta_1^2\theta_2^2) \tag{8}$$

where λ, θ_1, θ_2, and ϕ are the wavelength, sun and view zenith angles, and the relative azimuth between the sun and view angles, respectively. φ_1 and φ_2 are the two first basis functions of Price [21]. In Table I, the r_{s2}, r_{s3}, and r_{s4} values are fixed [10]. Only the view angle at nadir ($\theta_2 = 0$; $\phi = 0$) was considered. Soil reflectance is primarily controlled by r_{s1} (0 to 1.0).

2) Scenario 2 (SN2): In this scenario, the soil reflectance is based on the minimum and maximum soil reflectances measured in the field. It has been shown that the range of reflectance values for a given soil due to different soil moisture conditions is often greater than that found between soils of different taxonomic classes [42]. For a particular soil type, soil moisture content governs the magnitude of the soil spectral reflectance, whereas the overall shape of the spectral reflectance curve seems to be unaffected by varying moisture conditions. Soil reflectance is calculated with

$$\rho_{is} = \rho_{i1} + (\rho_{i2} - \rho_{i1}) * \text{RI} \tag{9}$$

where ρ_{i1} and ρ_{i2} are the minimum (wet soil) and maximum (dry soil) reflectances at band i. RI is the magnitude of the soil spectral reflectance between the minimum and maximum reflectances. The major soil types in the BARC area are represented by Codorus and Othello. The soil reflectance database of Codorus (Fig. 2) was created from topsoil samples as part of a study by Daughtry [43]. The wet and dry soil reflectances reported here were measured in the laboratory. The spectral response of these soils when covered by canopy litter is not known.

3) Scenario 3 (SN3): For simplification, soil reflectance is assumed to be constant over the spectrum, and the magnitude of
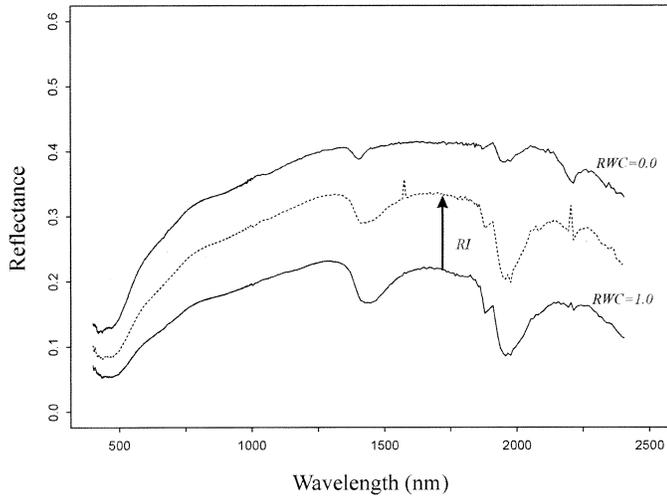
Fig. 2. Spectral reflectance of Codorus at a range of relative water contents (RWC) from oven dry (RWC = 0.0) to water saturated (RWC = 1.0).

the reflectance changes with soil moisture. Among the five representative mineral soil reflectance spectra [44], the iron-dominated soil (high ion content, fine texture) is the only one that has very little variation over the spectrum. It is not our contention that this scenario represents all soil types. Its purpose is to test the viability of the NN method. In this simulation, soil reflectance varies from 0 to 1.0.

C. Creating the Databases

Together with SRI, Kuusk's forward model MCRM was run with variable θ_1 and LAI for the three comparison scenarios that required modifications to the MCRM soil reflectance calculation. SN1 makes use of the default r_{s1} in Kuusk's model. For SN2, SN3, and SRI, the canopy model code needed to be revised. SN2 uses the measured minimum and maximum reflectance data. SN3 just assumes a common soil reflectance (varies within 0 to 1.0) for all bands. SRI, derived from the soil line of the red–NIR spectral space, reflects the instantaneous soil reflectance acquired from satellite data. Besides soil reflectance, all other parameters were the same for SRI, SN1, SN2, and SN3. The parameters were fixed with the following values: $S_L = 0.15$, $C_n = 0.95$, $C_w = 0.01$ cm, $C_p = 0.001$ g/cm^2, $C_c = 0.002$ g/cm^2 [45], $r_{s2} = 0.02$, and the leaf orientation was assumed to be spherical ($e = 0$; $\theta_m = 0$) (Table I). The output is nadir reflectance in the 400–2500-nm range with a spectral resolution of 5 nm. The reflectance was integrated into Landsat ETM+ bands with the sensor spectral response function. Four LUTs were constructed from the reflectance simulations for neural network training and prediction.

The second database was based on the TOA radiance. In order to explicitly model the physical state of the land surface, the surface bidirectional reflectance distribution function (BRDF) was used in this paper. Earlier studies [46], [47] found significant differences between radiances at TOA over natural surfaces and their Lambertian model equivalent, even though their albedos were equal. Other studies [48], [49] that investigated the interactions between the atmosphere and an underlying non-Lambertian surface also found that the use of the Lambertian assumption could result in a considerable amount of error in an upward radiance calculation from satellite.

For database 2, we simulated the TOA radiance L_t using an approximate expression [50]

$$L_t = L_p + \frac{T_p F \rho_e}{1 - S\overline{\overline{\rho}}} \tag{10}$$

where L_p is the atmospheric path radiance; T_p is the atmospheric transmittance of the atmosphere between the ground surface and the sensor; F is the downwelling radiative flux above the surface of zero reflectance; S is the fraction of surface radiance reflected by the atmosphere back to the surface; and ρ_e is the effective spectral reflectance of the surface expressed by

$$\rho_e = b\rho_L(\mu_s) + (1 - b)\overline{\overline{\rho}} \tag{11}$$

$$b = \frac{\exp\left\{-\left[1 - (1 - S^3)(\mu_s - 0.5)\right]\tau/\mu_s\right\}}{T_p}. \tag{12}$$

ρ_L is regarded as the equivalent Lambertian albedo [50], and $\overline{\overline{\rho}}$ is approximated by the hemispherical albedo of the surface as in [51].

There are two types of coefficients in (10)—atmosphere related (L_p, S, T_p, and F) and surface related (ρ_e and $\overline{\overline{\rho}}$). Atmospherically related coefficients were calculated using an atmospheric RT model (MODTRAN 4.0) based on a Lambertian assumption. Five atmospheric visibility values (2, 5, 10, 50, and 200 km) were used to reflect different aerosol loadings. The midlatitude rural atmospheric profile was applied. The atmospheric water vapor content varied from 0.0–3.0 cm (0.0, 0.5, 1.0, 2.0, and 3.0 cm). A range of solar zenith angles (SZAs) was simulated from 10° to 70° at a 10° increment. Surface coefficients were determined from the BRDF simulation—regardless of atmospheric conditions—because surface BRDF is an intrinsic property of the surface [52]. The parameters ρ_e and $\overline{\overline{\rho}}$ were derived from the MCRM model with minor modifications. After determining L_p, S, T_p, and F, the TOA radiance was calculated by (10).

D. Estimating LAI With the NN Method

Different ETM+ band combinations could be used to invert LAI from an RT model with the NN method. We used all data points in the two databases to train the NN. ETM+ reflectance, radiance, and field-measured LAI were used in the verification process. The training and checking data sets included reflectances in the green, red, NIR, and middle-infrared (MIR) spectral region as well as computed NDVI (Table III for database 1). The green, red, NIR, and MIR band radiances were also used for the training and checking of database 2. [NDVI for database 2 was calculated using red and NIR radiances following (1).] The R-square value and rms error (RMSE) were calculated for different scenarios and SRI for each band combination. We did not exhaust all possible band combinations, but did evaluate the most commonly used bands.

The computations were performed using the Splus neural network tool [53]. After identifying the best band combination, the training process was conducted with the corresponding LUT and field measurements were used for verification. The best band combination was used to map LAI from the ETM+ imagery.

TABLE III
COMPARISON OF R-SQUARE AND RMSE FOR DIFFERENT NEURAL NETWORK SCENARIOS AND THE APPLICATION OF THE SRI.
BAND COMBINATIONS USING SURFACE REFLECTANCES SIMULATED FROM MCRM

BAND COMBINATION	SN1		SN2		SN3		SRI	
	R^2	RMSE	R^2	RMSE	R^2	RMSE	R^2	RMSE
2, 3	0.4023	1.6349	0.2101	2.7	0.6075	1.6784	0.5522	1.6389
2, 4	0.7722	1.032	0.6236	1.7824	*0.8361*	*0.725*	0.7536	1.6655
2, 5	0.1054	2.3065	0.0161	4.2217	0.0447	2.1306	0.0139	2.0362
2, NDVI	0.7459	1.1813	0.7264	1.087	0.7196	1.2436	*0.7378*	*0.9916*
3, 4	0.8081	1.1332	0.6816	1.3071	0.8137	0.9254	*0.8015*	*0.8095*
3, 5	0.3062	2.6583	0.0245	3.1032	0.0716	2.0174	0.1333	1.9811
3, NDVI	0.8013	1.1285	0.7383	1.1772	*0.8101*	*0.9192*	*0.7952*	*0.8508*
4, 5	0.6078	19.161	0.7158	18.095	0.7803	3.7898	0.8196	4.9209
4, NDVI	0.8115	1.1009	*0.7967*	*0.9494*	*0.816*	*0.8942*	*0.8021*	*0.8048*
5, NDVI	0.5332	2.145	0.0261	3.2974	0.5214	1.7316	0.5452	1.5214
2, 3, 4	0.4571	1.2638	*0.7709*	*0.9387*	*0.7925*	*0.9132*	*0.7742*	*0.9551*
2, 3, 5	0.3488	20.071	0.0401	9.285	0.2154	3.651	0.0581	5.3729
2, 3, NDVI	0.561	1.4124	0.7399	1.0352	0.7319	1.3805	*0.7597*	*0.9063*
2, 4, 5	0.0552	14.559	0.0725	13.155	0.0151	11.36	0.2765	17.423
2, 4, NDVI	0.2106	2.7003	0.0901	2.6999	*0.8247*	*0.8444*	0.745	1.066
2, 5, NDVI	0.6934	1.6588	0.3775	2.0413	0.4265	1.7554	0.4953	1.5194
3, 4, 5	0.0038	40.357	0.3078	32.144	0.0689	12.806	0.5972	19.22
3, 4, NDVI	0.8071	1.106	*0.7996*	*0.9806*	*0.8141*	*0.9019*	*0.8051*	*0.8022*
3, 5, NDVI	0.051	8.7336	0.3346	2.1553	0.2037	2.0226	0.3095	2.6856
4, 5, NDVI	0.6387	31.337	0.0377	2.28	0.0705	7.1147	0.2002	27.52
2, 3, 4, 5	0.029	26.226	0.2964	10.917	0.1435	5.2947	0.3338	7.2955
2, 3, 4, NDVI	0.3378	1.4478	0.2846	2.7	0.0042	2.7001	0.6949	1.2642
2, 3, 5, NDVI	0.2933	6.4625	0.3254	2.2912	0.0002	2.0724	0.7848	1.2787
2, 4, 5, NDVI	0.5788	1.6387	0.5299	20.077	0.6317	8.4994	0.0872	27.467
3, 4, 5, NDVI	0.7551	18.533	0.4793	25.14	0.0916	1.8153	0.7141	3.2424
2, 3, 4, 5, NDVI	0.2053	18.157	0.0818	12.027	0.145	6.5945	0.159	2.6857

IV. RESULTS AND ANALYSIS

A. LAI Retrieval From ETM+ Surface Reflectance

In Table III, all RMSE < 1.0 are italicized. For SN1, all of the RMSEs are greater than 1.0. For SN2, three combinations have an RMSE < 1.0, while for SN3, six band combinations had that value. The best results were observed for the SRI that had seven RMSE < 1.0. Including NDVI improved the retrieval accuracy to some extent. For example, the R^2/RMSE for the band combinations of (2, 3), (2, 4), and (2, 5) are 0.55/1.64, 0.75/1.67, and 0.01/2.04, while R^2/RMSE for (2, 3, NDVI), (2, 4, NDVI), and (2, 5, NDVI) are 0.76/0.91, 0.75/1.07, and 0.50/1.52. Because NDVI incorporates the information content of bands 3 and 4, the R^2/RMSE of (3, 4) and (3, 4, NDVI) were almost the same. In addition, the introduction of green band (i.e., band 2) did not improve the results. The R^2/RMSE for (3, NDVI) and (4, NDVI) decreased from 0.80/0.85 and 0.80/0.80 to 0.76/0.91 and 0.75/1.07 when band 2 was used. Moreover, poor results (RMSE > 1.0) were obtained when band 5 was used, and unacceptable results occurred when more than four bands (NDVI as a separate band) were used.

B. LAI Retrieval From ETM+ Raw Radiance

The results of LAI retrieval from the ETM+ raw radiance are displayed in Table IV (RMSE < 1.5 are italicized). Similar to Table III results, there is no combination for SN1 whose RMSE is less than 1.5. This implies that SN1 may not be appropriate for TOA radiance calculation. In addition, only one RMSE was less than 1.5 for the TOA radiance with SN2. This is not surprising, since the laboratory-measured soil reflectance did not fully represent actual field conditions. Errors were also introduced because database 2 was calculated from an empirical (10). For SN3, there is only one combination (4, NDVI) with an RMSE < 1.5. The best results were seen with the combination of band 4 (NIR) and NDVI ($R^2 = 0.74$, RMSE $= 1.17$) for SRI, which suggests this band combination should be used for estimating LAI from TOA radiance. These results may be explained by the fact that visible bands are significantly affected by atmospheric conditions, while infrared bands are not. Moreover, NDVI is not significantly affected by atmospheric effects because these factors are normalized out in the process of its calculation [54].

Similar to database 1, the results were very poor when the combination used more than four bands. The effect of adding NDVI varies with different band combinations. For most cases, using NDVI did not improve the results. The introduction of green band radiance deteriorated the results to some extent and the effect of band 5 was also negative—all RMSE > 1.5 when band 5 was used.

TABLE IV
SAME TO TABLE III, BUT USING TOA RADIANCE IN BAND COMBINATIONS

BAND COMBINATION	SN1		SN2		SN3		SRI	
	R^2	RMSE	R^2	RMSE	R^2	RMSE	R^2	RMSE
2, 3	0.1700	5.2625	0.0223	40.4603	0.0822	67.5674	0.0438	29.2868
2, 4	0.0391	2.0105	0.0002	2.3056	0.0648	2.1652	0.1048	2.2036
2, 5	0.0702	4.3581	0.0712	3.0718	0.0690	2.3562	0.0816	2.2777
2, NDVI	0.5557	2.1632	0.5397	24.3915	0.2150	22.6303	0.4674	3.4295
3, 4	0.4003	2.1518	*0.6235*	*1.3118*	0.6955	1.6551	0.4408	1.7748
3, 5	0.0052	2.2525	0.0312	2.8464	0.0826	2.6193	0.0159	2.3495
3, NDVI	0.6699	1.9020	0.5193	2.4603	0.5755	1.8780	0.3285	1.9902
4, 5	0.0090	6.0347	0.0027	5.6974	0.0174	7.4843	0.0004	55.4644
4, NDVI	0.2131	2.3706	0.6385	1.5869	*0.7372*	*1.2019*	*0.7442*	*1.1701*
5, NDVI	0.0010	2.1486	0.0307	2.6477	0.0303	2.5607	0.0603	2.6699
2, 3, 4	0.0156	1.7759	0.0121	2.0391	0.0568	1.7057	0.0012	1.9701
2, 3, 5	0.0307	4.0950	0.0040	5.3889	0.0833	84.7633	0.0932	3.0354
2, 3, NDVI	0.0891	2.9434	0.6875	11.2830	0.4711	75.9847	0.0447	68.7834
2, 4, 5	0.0479	5.3905	0.0694	4.4210	0.0885	4.5779	0.0079	4.9147
2, 4, NDVI	0.5549	2.2269	0.4978	2.6760	0.6466	3.9618	0.6875	2.8680
2, 5, NDVI	0.0219	17.4510	0.4069	9.7468	0.0049	8.7707	0.5951	10.6470
3, 4, 5	0.0462	6.0392	0.0094	4.9709	0.0098	11.2123	0.0013	5.5459
3, 4, NDVI	0.6377	1.8139	0.5693	1.7601	0.3793	1.7854	0.5496	1.7832
3, 5, NDVI	0.0180	5.5558	0.1570	1.9513	0.6091	1.6705	*0.5330*	*1.4873*
4, 5, NDVI	0.0000	4.3379	0.0021	27.1991	0.5849	1.9930	0.5401	3.0628
2, 3, 4, 5	0.0659	5.1442	0.1017	3.7472	0.0097	6.4394	0.1030	3.4869
2, 3, 4, NDVI	0.1840	2.5507	0.1762	2.0701	0.3513	15.2807	0.0490	2.4762
2, 3, 5, NDVI	0.1361	5.8437	0.0120	162.7613	0.0383	159.8680	0.0343	108.8274
2, 4, 5, NDVI	0.0148	6.0143	0.1189	44.0487	0.0681	55.9402	0.5703	59.6755
3, 4, 5, NDVI	0.0615	5.4126	0.4532	80.8209	0.0944	45.6471	0.2572	37.4586
2, 3, 4, 5, NDVI	0.0001	4.6033	0.0014	45.7972	0.0001	129.6289	0.0086	28.8632

For SN2, SN3, and SRI, database 1 performed much better than database 2. It is not surprising that LAI could be better estimated from atmospherically corrected surface reflectance data than from raw TOA radiances. Similar results were reported by [15], which used both reflectance and radiance to calculated VIs and found that the LAI–VI relationships based on reflectance data were stronger than those based on radiance data. In this analysis, a perfect atmospheric correction has been assumed for database 1. Yet, if it is believed that atmospheric correction introduced large uncertainties to the surface reflectance, the second scheme might be a better solution.

The best results were obtained from (3, 4) in database 1 with the SRI method. Therefore, Landsat ETM+ reflectances in the red and NIR were picked to map LAI with the trained NN. The strategy behind this selection was based on choosing the best R^2 and RMSE as well as considering computation efficiency. This result was also obtained by [28]. All simulated points in the LUT were used to train the NN that was then applied to Landsat ETM+ red and NIR reflectances to predict LAI.

C. Validation

To validate the proposed approach, the NN-derived LAIs were compared with field measurements. Fig. 3 shows that the SRI method performs well ($R^2 = 0.801$, RMSE = 0.811) in

estimating LAI. The constant soil reflectance approach in SN3 also performs well ($R^2 = 0.814$, RMSE = 0.925). The NN method tends to underestimate LAI for both SN1 and SN2. Using SN1 seems unrealistic, and SN2 is not representative for this study area. Although Kuusk [55] mentioned that MCRM may not work well for forests, most of the retrieved forest LAIs agreed well with the field-measured green LAIs (Fig. 4). Among the four options, the largest deviation is seen in SN2 (Fig. 4).

Errors caused by model simulation, sensor calibration, or measurement should be taken into account. To test the sensitivity of the neural network approach to uncertainty in the input reflectance, three bias levels ($\pm 15\%$, $\pm 10\%$, and $\pm 5\%$) were generated for evaluation. The relative errors were added to the ETM+ surface reflectance and TOA radiance dataset. The relative R^2 and RMSE differences were calculated between the biased and the original datasets

$$(\mathbf{R'} - \mathbf{R})/\mathbf{R}$$

where $\mathbf{R}$, and $\mathbf{R'}$ are the R^2 or RMSE obtained using the original and biased datasets, respectively. Table V lists the relative R^2 and RMSE differences using SRI. This table includes those band combinations that performed well—bands 3 and 4 for surface reflectance and 4, NDVI for TOA radiance.
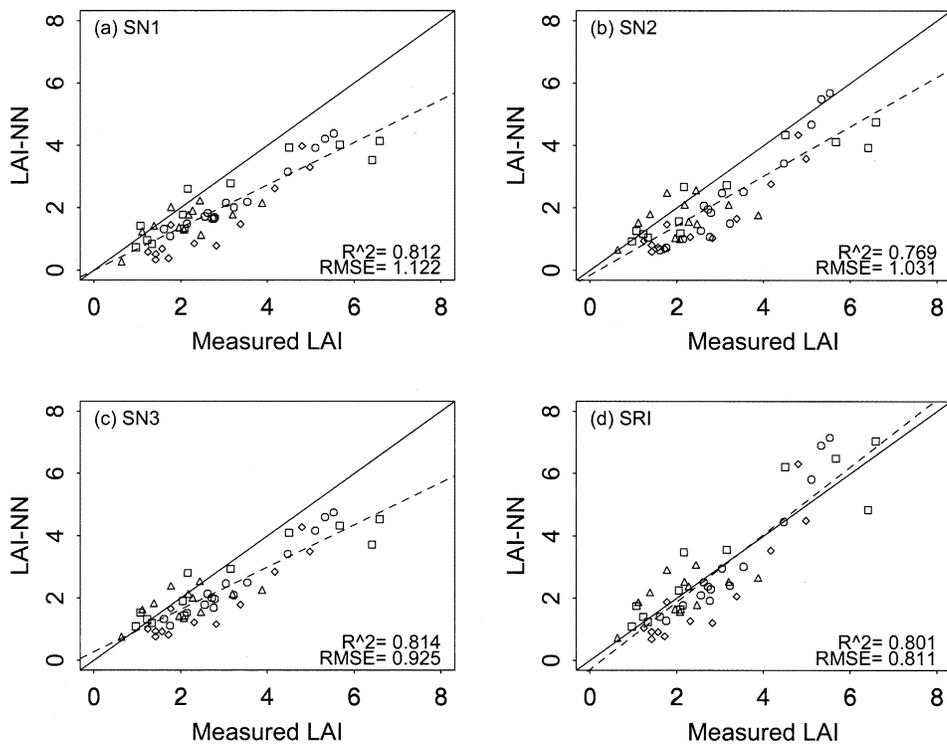
Fig. 3. Comparison of LAI–NN with field LAI. LAI–NN is estimated from the Landsat ETM+ images with the neural network methods for four different soil backgrounds (options). (a) SN1, (b) SN2, (c) SN3, and (d) SRI. R^2: R square. Symbols: May 11 (□), October 2 (○) 2000, April 28 (◇), and August 2 (△) 2001. The solid line is the 1 : 1 line, and the dashed one the regression line.
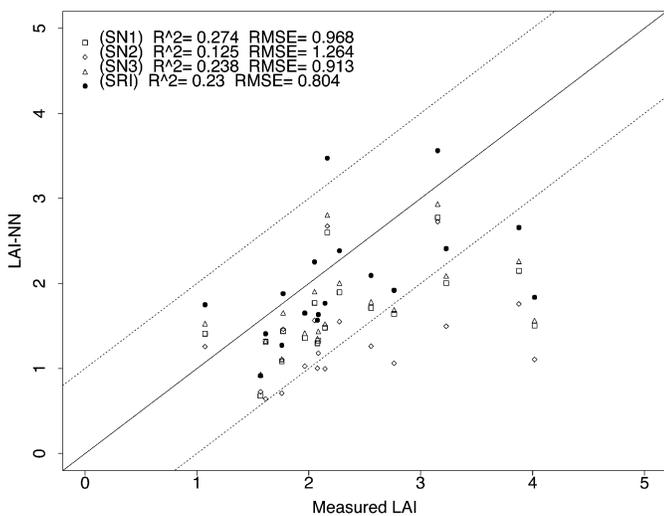
Fig. 4. Comparison of retrieved forest LAI–NN values from SN1 (□), SN2 (◇), SN3 (△), and the SRI (●), respectively, with field-meausred LAI. The intercepts of the dashed lines are ±1.

For the surface reflectance, the R^2 nearly keeps constant across different noise levels. The RMSE values are lower at low noise levels and are a little biased when the absolute biases are greater than 10%. This indicates that our approach is very robust to different reflectance noise levels and thus it lends itself to practical applications. On the other hand, the noise has significant effects on LAI estimated from TOA radiance. All

R^2 are much lower than the original values for different bias levels. The RMSE is lower at low noise levels but increases quickly when the noise increases. This is an indication that using TOA radiance maybe unrealistic for LAI estimation if there are too many uncertainties.

D. LAI Mapping

NN training results from the SRI (Fig. 3) were used to estimate LAI for four Landsat ETM+ images (Fig. 5). The May 11 and October 2, 2000 images are 512×512 and 600×600 pixels, respectively. The April 28 and August 2, 2001 images are both 300×300 pixels. In Fig. 5, white areas were either bare land or roads, and the gray-white areas were construction sites. The LAI of most crops and forests were between 2 to 6. The LAI maps correspond well with local landscape characteristics. Statistics from the LAI maps are shown in Table VI. May 11, 2000 and August 2, 2001 have the highest mean LAI values. The LAI standard deviation of May 11, 2000 is greater than that of August 2, 2001, which may be due to variability caused by differing planting and emergence dates. Most areas have LAI values less than 4.0 (Table VI). However, some dark pixels on the April 28, 2001 LAI–NN map were dense grasses with a LAI–NN greater than 6.0. Because this method was seen to provide accurate estimates of vegetation amount throughout the growing season, it is believed that this approach could be applied to a large area for regional LAI mapping. Fig. 6 provides an example of this application and is valuable for comparison with LAI products from other sensors such as MODIS or MISR.
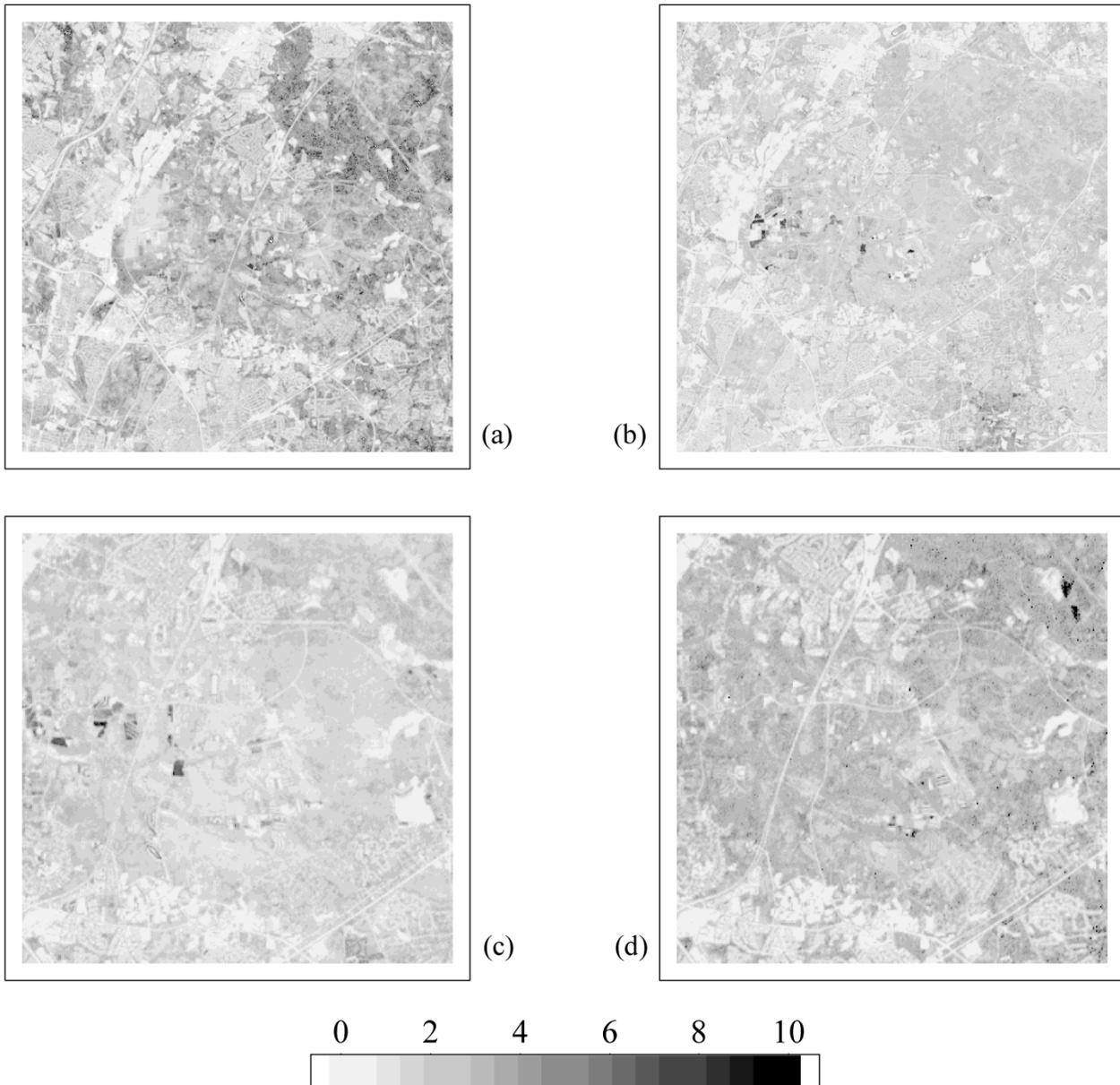
Fig. 5. LAI maps generated with the neural network method. (a) May 11, 2000. (b) October 2, 2000. (c) April 28, 2001. (d) August 2, 2001.

TABLE V

RELATIVE R^2 AND RMSE DIFFERENCES FOR DIFFERENT BIAS LEVELS. BAND (3, 4) WAS USED FOR SURFACE REFLECTANCE AND (4, NDVI) FOR TOA RADIANCE

Bias levels		-15%	-10%	-5%	+5%	+10%	+15%
(3,4)	R^2	0.0034	0.0035	0.0021	-0.0026	-0.0045	-0.0053
	RMSE	0.1282	-0.0051	-0.0521	0.1711	0.4091	0.6973
(4,NDVI)	R^2	-0.9219	-0.8547	-0.7469	-0.6293	-0.7174	-0.7729
	RMSE	0.8336	0.7151	0.6228	1.3337	3.2187	6.1858

V. SUMMARY

This paper has demonstrated how the neural network method can be used to retrieve LAI from the Landsat-7 ETM+ surface reflectance and TOA radiance. The NN was trained with two databases to test estimating LAI from atmospherically corrected surface reflectance (database 1) and raw TOA radiance (database 2). Database 1 was constructed with a canopy RT model and database 2 with the combined atmospheric and canopy RT

models. A soil reflectance index was proposed to account for soil background reflectance. To define the SRI, the shape of the soil-line in the red–NIR spectral space is needed. SRI minimizes the number of parameters involved in computing the soil spectral reflectance.

Our results show that LAI can be obtained through the NN approach from both surface reflectance and TOA radiance. The outputs were compared with field-measured LAI datasets from

TABLE VI
STATISTICS OF THE LAI–NN ESTIMATED FROM THE FOUR ETM+ REFLECTANCES

DATES	MINIMUM	MAXIMUM	MEAN LAI	STANDARD DEVIATION	LAI<4 PIXELS (%)
May 11, 2000	0 .0	6.39	2.28	1.31	91.43
Oct 2, 2000	0.0	6.44	1.54	0.76	99.5
Apr 28, 2001	0.0	6.22	1.57	0.68	99.45
Aug 2, 2001	0.0	8.81	2.26	0.97	98.15
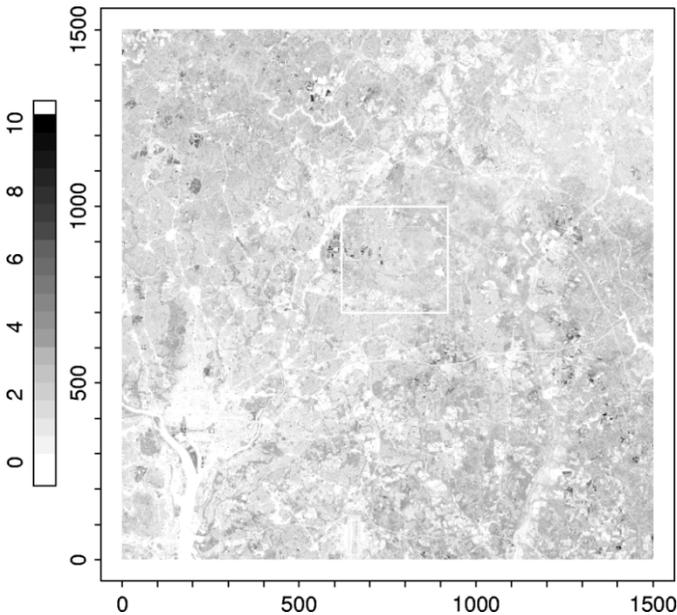
Fig. 6. LAI distribution estimated using the proposed approach with ETM+ for April 28, 2001 over the Washington, DC area. White box shows the Fig. 5(c) area. Size: 1500 × 1500 pixels.

four different dates. The surface reflectance approach resulted in an $R^2 = 0.801$ and RMSE $= 0.811$ using input bands 3 and 4. When the TOA radiance of band 4 and NDVI were used, the results were not as good: $R^2 = 0.74$, RMSE $= 1.17$. Estimating LAI from TOA radiance does, however, have the advantage of avoiding performing a complicated atmospheric correction process. In general, bands 3 and 4 are recommended for estimating LAI from ETM+ surface reflectance, while band 4 and NDVI are recommended if TOA radiance is used. The sensitivity experiment showed that our approach is very robust, especially when surface reflectance is used.

Extension of this method to other satellite data sources of different spatial resolutions is currently underway. LAI results derived from the high-resolution ETM+ image could be used to validate LAI products from low-resolution sensors (e.g., MODIS, MISR, and POLDER). There are several areas that need improvement in the future. The soil line was determined from the whole image in this study, but it may be advantageous to construct different soil lines from different parts of the image, especially when very complicated landscape exists. In multiple viewing angles simulations, soil reflectance is a very crucial parameter [13], and the significance of SRI needs further evaluation. Finally, more tests are needed to determine the best band combinations for application to new sensor systems.

REFERENCES

[1] J. M. Chen, "Evaluation of vegetation indices and a modified simple ratio for Boreal applications," *Can. J. Remote Sens.*, vol. 22, pp. 229–242, 1996.
[2] CEOS/WMO. Satellite systems and requirements (the official CEOS/WMO online database). [Online]. Available: http://alto-stratus.wmo.ch/sat/stations/SatSystem.html.
[3] S. D. Prince, "What practical information about land-surface function can be determined by remote sensing? Where do we stand?," in *Integrating Hydrology, Ecosystem Dynamics, and Biogeochemistry in Complex Landscapes*, J. D. Tenhunen and P. Kabat, Eds. New York: Wiley, 1999, pp. 39–60.
[4] S. Liang, *Quantitative Remote Sensing of Land Surfaces*. New York: Wiley, 2003.
[5] N. Gobron, B. Pinty, and M. M. Verstraete, "Theoretical limits to the estimation of the leaf area index on the basis of visible and near-infrared remote sensing data," *IEEE Trans. Geosci. Remote Sensing*, vol. 35, pp. 1438–1445, Nov. 1997.
[6] R. B. Myneni, R. Ramakrishna, R. Nemani, and S. W. Running, "Estimation of global leaf area index and absorbed par using radiative transfer models," *IEEE Trans. Geosci. Remote Sensing*, vol. 35, pp. 1380–1393, Nov. 1997.
[7] C. O. Justice, E. Vermote, J. R. G. Townshend, R. Defries, D. P. Roy, D. K. Hall, V. V. Salomonson, J. L. Privette, G. Riggs, A. Strahler, W. Lucht, R. B. Myneni, Y. Knyazikhin, S. W. Running, R. R. Nemani, Z. Wan, A. R. Huete, and W. van Leeuwen, "The Moderate Resolution Imaging Spectroradiometer (MODIS): Land remote sensing for global change research," *IEEE Trans. Geosci. Remote Sensing*, vol. 36, pp. 1228–1249, July 1998.
[8] Y. Knyazikhin, J. Glassy, J. L. Privette, Y. Tian, A. Lotsch, Y. Zhang, Y. Wang, J. T. Morisette, P. Votava, R. B. Myneni, R. R. Nemani, and S. W. Running, "MODIS leaf area index (LAI) and fraction of potosynthetically active radiation aborbed by vegetation (FPAR),", Product (MOD15) Algorithm Theoretical Basis Doc., 1999.
[9] Y. Knyazikhin, J. V. Martonchik, D. J. Diner, R. B. Myneni, M. Verstraete, B. Pinty, and N. Gobron, "Estimation of vegetation canopy leaf area index and fraction of absorbed photosynthetically active radiation from MISR data," *J. Geophys. Res.*, vol. 103, pp. 32,239–32 256, 1998.
[10] P. Bicheron and M. Leroy, "A method of biophysical parameter retrieval at global scale by inversion of a vegetation reflectance model," *Remote Sens. Environ.*, vol. 67, pp. 251–266, 1999.
[11] P. Bicheron, M. Leroy, and O. Hautecoeur, "LAI and fAPAR mapping at global scale by model inversion against spaceborne POLDER data," in *Proc. IGRASS*, 1998.
[12] D. S. Kimes, Y. Knyazikhin, J. L. Privette, A. A. Abuelgasim, and F. Gao, "Inversion methods for physically-based models," *Remote Sens. Rev.*, vol. 18, pp. 381–440, 2000.
[13] D. Kimes, J. Gastellu-Etchegorry, and P. Estève, "Recovery of forest canopy characteristics through inversion of a complex 3D model," *Remote Sens. Environ.*, vol. 79, pp. 320–328, 2002.
[14] J. A. Smith, "LAI inversion using a backpropagation neural network trained with a multiple scattering model," *IEEE Trans. Geosci. Remote Sensing*, vol. 31, pp. 1102–1106, Sept. 1993.
[15] D. P. Turner, W. B. Cohen, R. E. Kennedy, K. S. Fassnacht, and J. M. Briggs, "Relationships between leaf area index and landsat TM spectral vegetation indices across three temperate zone sites," *Remote Sens. Environ.*, vol. 70, pp. 52–68, 1999.

[16] S. Liang, "A direct algorithm for estimating land surface broadband albedos from MODIS imagery," *IEEE Trans. Geosci. Remote Sensing*, vol. 41, pp. 136–145, Jan. 2003.

[17] W. Qin and S. Liang, "Plane-parallel canopy radiation transfer modeling: Recent advances and future directions," *Remote Sens. Rev.*, vol. 18, pp. 281–306, 2000.

[18] M. Weiss and F. Baret, "Evaluation of canopy biophysical variable retrieval performances from the accumulation of large swath satellite data," *Remote Sens. Environ.*, vol. 70, pp. 293–306, 1999.

[19] A. Kuusk, "A Markov chain model of canopy reflectance," *Agricul. Forest Meteorol.*, vol. 76, pp. 221–236, 1995.

[20] T. Nilson and A. Kuusk, "A reflectance model for the homogeneous plant canopy and its inversion," *Remote Sens. Environ.*, vol. 27, pp. 157–167, 1989.

[21] J. C. Price, "On the information content of soil reflectance spectra," *Remote Sens. Environ.*, vol. 33, pp. 113–121, 1990.

[22] A. Kuusk, "A fast invertible canopy reflectance model," *Remote Sens. Environ.*, vol. 51, pp. 342–350, 1995.

[23] H. Fang and S. Liang, "Retrieving leaf area index (LAI) from a canopy radiative transfer model using a genetic algorithm," *Remote Sens. Environ.*, vol. 85, pp. 257–270, 2003.

[24] A. A. Abuelgasim, S. Gopal, and A. H. Strahler, "Forward and inverse modeling of canopy directional reflectance using a neural network," *Int. J. Remote Sens.*, vol. 19, pp. 453–471, 1998.

[25] X. Li and A. H. Strahler, "Geometric-optical bidirectional reflectance modeling of the discrete crown vegetation canopy: Effect of crown shape and multual shadowing," *IEEE Trans. Geosci. Remote Sensing*, vol. 30, pp. 276–292, Mar. 1992.

[26] J. Qi, Y. H. Kerr, M. S. Moran, M. Weltz, A. R. Huete, S. Sorooshian, and R. Bryant, "Leaf area index estimates using remotely sensed data and BRDF models in a semiarid region," *Remote Sens. Environ.*, vol. 73, pp. 18–30, 2000.

[27] N. H. Broge and E. Leblanc, "Comparing prediction power and stability of broadband and hyperspectral vegetation indices for estimation of green leaf area index and canopy chlorophyll density," *Remote Sens. Environ.*, vol. 76, pp. 156–172, 2001.

[28] F. Baret, J. Clevers, and M. Steven, "The robustness of canopy gap fraction estimates from red and near-infrared reflectances: A comparison of approaches," *Remote Sens. Environ.*, vol. 54, pp. 141–151, 1995.

[29] F. Baret and T. Fourty, "Estimation of leaf water content and specific leaf weight from reflectance and transmittance measurements," *Agronomie*, vol. 17, pp. 455–464, 1997.

[30] Y. Jin and C. Liu, "Biomass retrieval from high dimensional active/passive remote data by using artificial neural networks," *Int. J. Remote Sens.*, vol. 18, pp. 971–979, 1997.

[31] P. Gong, S. X. Wang, and S. Liang, "Inverting a canopy reflectance model using a neural network," *Int. J. Remote Sens.*, vol. 20, pp. 111–122, 1999.

[32] S. Liang and A. H. Strahler, "An analytic BRDF model of canopy radiative transfer and its inversion," *IEEE Trans. Geosci. Remote Sens.*, vol. 31, pp. 1081–1092, 1993.

[33] ASD, *FieldSpec Pro User's Guide*. Boulder, CO: Analytical Spectral Devices Corp., 2000.

[34] LAI-COR, *LAI-2000 Plant Canopy Analyzer: Operating Manual*, 1991, pp. 4–14.

[35] M. S. Moran, R. D. Jackson, P. N. Slater, and P. M. Teillet, "Evaluation of simplified procedures for retrieval of land surface reflectance factors from satellite sensor output," *Remote Sens. Environ.*, vol. 41, pp. 169–184, 1992.

[36] A. Berk, G. P. Anderson, P. K. Acharya, J. H. Chetwynd, L. S. Bernstein, E. P. Shettle, M. W. Matthew, and S. M. Adler-Golden, *MODTRAN4 Users Manual*. Hanscom AFB, MA: Hanscom AFB, Air Force Research Lab., 1999.

[37] B. N. Holben, T. Eck, I. Slutsker, T. Tanre, J. Buis, A. Setzer, E. Vermote, J. Reagan, Y. Kaufman, T. Nakajima, L. F. , I. Jankowiak, and A. Smirnov, "AERONET—A federated instrument network and data archive for aerosol characterization," *Remote Sens. Environ.*, vol. 66, pp. 1–16, 1998.

[38] S. Liang, H. Fang, and M. Chen, "Atmospheric correction of landsat ETM+ land surface imagery: I. Methods," *IEEE Trans. Geosci. Remote Sensing*, vol. 39, pp. 2490–2498, Nov. 2001.

[39] S. Liang, H. Fang, J. Morisette, M. Chen, C. Walthall, C. Daughtry, and C. Shuey, "Atmospheric correction of landsat ETM+ land surface imagery: II. Validation and applications," *IEEE Trans. Geosci. Remote Sensing*, vol. 40, pp. 2736–2746, Dec. 2002.

[40] F. Baret, S. Jacquemoud, and J. F. Hanocq, "The soil line concept in remote sensing," *Remote Sens. Rev.*, vol. 7, pp. 65–82, 1993.

[41] A. R. Huete, D. F. Post, and R. D. Jackson, "Soil spectral effects on 4-space vegetation discrimination," *Remote Sens. Environ.*, vol. 15, pp. 155–165, 1984.

[42] E. Muller and H. Décamps, "Modeling soil moisture-reflectance," *Remote Sens. Environ.*, vol. 76, pp. 173–180, 2001.

[43] C. S. Daughtry, "Discriminating crop residues from soil by shortware infrared reflectance," *Agronomy J.*, vol. 93, pp. 125–131, 2001.

[44] E. R. Stoner, "Physicochemical, site, and bidirectional reflectance factor characteristics of uniformly moist soils," Purdue Univ., W. Lafayette, IN, 1979.

[45] S. Jacquemoud, S. L. Ustin, J. Verdebout, G. Schmuck, G. Andreoli, and B. Hosgood, "Estimating leaf biochemistry using the PROSPECT leaf optical properties model," *Remote Sens. Environ.*, vol. 56, pp. 194–202, 1996.

[46] P. Koepke and K. T. Kriebel, "Influence of measured reflection properties of vegetated surfaces on atmospheric radiance and its polarization," *Appl. Opt.*, vol. 17, pp. 260–264, 1978.

[47] K. L. Coulson, E. L. Gray, and G. M. B. Bouricius, "Effect of surface reflection on planetary albedo," *Icarus*, vol. 5, pp. 139–148, 1966.

[48] D. Tanré, M. Herman, and P. Y. Deschamps, "Influence of the atmosphere on space measurements of directional properties," *Appl. Opt.*, vol. 22, pp. 733–741, 1983.

[49] T. Lee and Y. J. Kaufman, "The effect of surface nonlambertianity on remote sensing of ground reflectance and vegetation index," *IEEE Trans. Geosci. Remote Sensing*, vol. 24, pp. 699–708, 1986.

[50] J. Qiu, "An improved model of surface BRDF-atmospheric coupled radiation," *IEEE Trans. Geosci. Remote Sensing*, vol. 39, pp. 181–187, Jan. 2001.

[51] E. F. Vermote, D. Tanre, J. L. Deuze, M. Herman, and J. J. Morcrette, "Second simulation of the satellite signal in the solar spectrum, 6S: An overview," *IEEE Trans. Geosci. Remote Sensing*, vol. 35, pp. 675–686, May 1997.

[52] W. Qiu, J. R. Herman, and Z. Ahmad, "A fast, accurate algorithm to account for non-Lambertian surface effects on TOA radiance," *J. Geophys. Res.*, vol. 106, pp. 22 671–22 684, 2001.

[53] W. N. Venables and B. D. Ripley, *Modern Applied Statistics with S-PLUS*. New York: Springer-Verlag, 1994.

[54] Y. J. Kaufman and D. Tanré, "Atmospherically resistant vegetation index (ARVI) for EOS-MODIS," *IEEE Trans. Geosci. Remote Sensing*, vol. 30, pp. 261–270, Mar. 1992.

[55] A. Kuusk, "Monitoring of vegetation parameters on large areas by the inversion of a canopy reflectance model," *Int. J. Remote Sens.*, vol. 19, pp. 2893–2905, 1998.
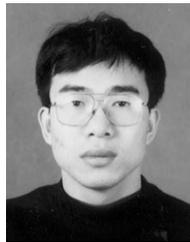
Hongliang Fang received the B.S. degree in geography from East China Normal University, Shanghai, China, in 1993, and the M.S. degree in cartography and GIS from the Institute of Geography, Chinese Academy of Sciences, Beijing, China, in 1996. He is currently pursuing the Ph.D. degree at the University of Maryland, College Park.

His previous interest was on use of remote sensing and GIS in a variety of fields such as environment monitoring, land cover/use, biomass monitoring, and wetland ecology. His most recent interest is in retrieving land surface parameters from remotely sensed data.

Shunlin Liang (M'94–SM'00) received the Ph.D. degree in remote sensing and GIS from Boston University, Boston, MA.

He was a Postdoctoral Research Associate at Boston University from 1992 to 1993, and a Validation Scientist of the NOAA/NASA Pathfinder AVHRR Land Project from 1993 to 1994. He is currently an Associate Professor at the University of Maryland, College Park. His present research interests focus on land surface data assimilation, parameter retrieval from remotely sensed data, and spatial analysis.

Dr. Liang organized the International Forum on BRDF at San Francisco, CA, in December 1998, and coedited a special issue of the *Remote Sensing Reviews*. He has chaired various sessions of the international conferences and served as the chairman of the IEEE Geoscience and Remote Sensing Society, Washington/North Virginia Chapter (2000). He is an Associate Editor of the IEEE TRANSACTIONS ON GEOSCIENCE AND REMOTE SENSING.